

Article

Plastic Waste Precursor-Derived Fluorescent Carbon and Construction of Ternary FCs@CuO@TiO₂ Hybrid Photocatalyst for Hydrogen Production and Sensing Application

Akansha Mehta ^{1,*}, Rayees Ahmad Rather ^{2,3}, Blaz Belec ⁴, Sandra Gardonio ⁴, Ming Fang ² and Matjaz Valant ^{4,5}

¹ FunGlass, A. Dubček University of Trenčín, Študentská 2, 911 50 Trenčín, Slovakia

² College of Material Science and Engineering, Shenzhen University, Shenzhen 518060, China; rrather85@gmail.com (R.A.R.); m.fang@szu.edu.cn (M.F.)

³ College of Physics and Optoelectronic Engineering, Shenzhen University, Shenzhen 518060, China

⁴ Materials Research Laboratory, University of Nova Gorica, Vipavska 11c, 5270 Ajdovscina, Slovenia; blaz.belec@ung.si (B.B.); sandra.gardonio@ung.si (S.G.); matjaz.valant@ung.si (M.V.)

⁵ Institute of Fundamental and Frontier Sciences, University of Electronic Science and Technology of China, Chengdu 610054, China

* Correspondence: akansha.akansha@tuni.sk; Tel.: +421-951561593



Citation: Mehta, A.; Rather, R.A.; Belec, B.; Gardonio, S.; Fang, M.; Valant, M. Plastic Waste Precursor-Derived Fluorescent Carbon and Construction of Ternary FCs@CuO@TiO₂ Hybrid Photocatalyst for Hydrogen Production and Sensing Application. *Energies* **2022**, *15*, 1734. <https://doi.org/10.3390/en15051734>

Academic Editor: Dmitri A. Bulushev

Received: 11 January 2022

Accepted: 23 February 2022

Published: 25 February 2022

Publisher's Note: MDPI stays neutral with regard to jurisdictional claims in published maps and institutional affiliations.



Copyright: © 2022 by the authors. Licensee MDPI, Basel, Switzerland. This article is an open access article distributed under the terms and conditions of the Creative Commons Attribution (CC BY) license (<https://creativecommons.org/licenses/by/4.0/>).

Abstract: A sustainable nexus between renewable energy production and plastic abatement is imperative for overall sustainable development. In this regard, this study aims to develop a cheaper and environmentally friendly nexus between plastic waste management, wastewater treatment, and renewable hydrogen production. Fluorescent carbon (FCs) were synthesized from commonly used LDPE (low-density polyethylene) by a facile hydrothermal approach. Optical absorption study revealed an absorption edge around 300 nm and two emission bands at 430 and 470 nm. The morphological analysis showed two different patterns of FCs, a thin sheet with 2D morphology and elongated particles. The sheet-shaped particles are 0.5 μm in size, while as for elongated structures, the size varies from 0.5 to 1 μm. The as-synthesized FCs were used for the detection of metal ions (reference as Cu²⁺ ions) in water. The fluorescence intensity of FCs versus Cu²⁺ ions depicts its upright analytical ability with a limit of detection (LOD) reaching 86.5 nM, which is considerably lesser than earlier reported fluorescence probes derived from waste. After the sensing of Cu²⁺, the as-obtained FCs@Cu²⁺ was mixed with TiO₂ to form a ternary FCs@CuO@TiO₂ composite. This ternary composite was utilized for photocatalytic hydrogen production from water under 1.5 AM solar light irradiation. The H₂ evolution rate was found to be ~1800 μmolg⁻¹, which is many folds compared to the bare FCs. Moreover, the optimized FCs@CuO@TiO₂ ternary composite showed a photocurrent density of ~2.40 mA/cm² at 1 V vs. Ag/AgCl, in 1 M Na₂SO₄ solution under the illumination of simulated solar light. The achieved photocurrent density corresponds to the solar-to-hydrogen (STH) efficiency of ~0.95%. The efficiency is due to the fluorescence nature of FCs and the synergistic effect of CuO embedded in TiO₂, which enhances the optical absorption of the composite by reaching the bandgap of 2.44 eV, apparently reducing the recombination rate, which was confirmed by optoelectronic, structural, and spectroscopic characterizations.

Keywords: plastic waste; fluorescent carbon; sensing of metal ions; photocatalytic hydrogen production

1. Introduction

Accumulation of waste plastic is a cause of concern due to its non-biodegradable nature and negative implications on environmental sustainability. Low-density polyethylene (LDPE) is mass-produced and commonly discharged after use in an open environment without any proper treatment [1,2]. Since LDPE contains polymeric carbon chains as a major constituent thus, its redesigning and fabrication into the carbon-based value-added

products is appreciated [3,4]. During recent years, among the carbon-based materials, fluorescent carbon (FCs) nanomaterials have attracted attention as new fluorescent probes for the sensing of toxic moieties from wastewater [5,6]. The selection is based on its low toxicity, photostability, and facile synthetic procedures [7–10]. Most published reports focus on the synthesis of carbon nanodots, graphene quantum dots, and other carbon-based materials, but only a few published reports are available on FCs discussing an in situ formation of nanocomposite for various environmental applications [11–13]. Furthermore, only a limited number of carbon precursors can be altered and rearranged into photoactive carbon structures [14–16]. In this regard, we choose linear low-density polyethylene (LLDPE) as base materials for the fabrication of FCs. The as-fabricated FCs were utilized for the sensing of metals (Cu^{2+}) from wastewater.

Water pollution by heavy metals is one of the biggest environmental problems in the last decades [17]. The choice of copper is based on the fact it is the most accumulated metal in wastewater because it is commonly used in many industrial applications such as the production of electrical conductors, alloys, plant protection products, and artificial fertilizers. Moreover, it can be accumulated in the water systems through the waste flows from the mines and metal processing plants [18–22]. Numerous methods were investigated for sensing heavy metals from wastewater, including atomic fluorescence spectrometry (AFS), potentiometric sensors, coupled plasma mass spectrometry (CPMS), and atomic absorption spectrometry (AAS) [17–22]. The above-mentioned techniques are time-consuming and require high-cost instrumentation, complex sampling, and the usage of toxic/hazardous chemicals [23,24]. Therefore, fluorescent carbon (FCs) based sensors could be promising for effective Cu^{2+} sensing. This method could prove to be a cost-effective strategy for creating a plastic waste-metal sensing nexus for sustainability. Though researchers have used various semiconducting materials for the sensing of toxic metals from wastewater, concerns still arise about their strategic disposal management [25,26]. According to the World Health Organization (WHO) and the world counts records, every year, 3,575,000 people die from water-related diseases. This is equivalent to a jumbo jet crashing every hour, and most of these people are children (2.2 million) [27,28]. The disproportion at the addition of heavy metals leads to a serious threat to human health and the environment, particularly in emerging and developing countries [29,30]. Furthermore, following the electroplating wastewater discharge standards, the acceptable concentrations of Cu^{2+} are 1 mg/L, and notably, the detection limits of FCs are far below these regulatory values, signifying their prospective application for the determination of Cu^{2+} ions in industrial wastewater [31].

In the current study, after sensing Cu^{2+} , the FCs@ Cu^{2+} interface is formed, which could be easily turned into a photocatalyst by mixing or immobilizing on some semiconductor surface. These mixed photocatalysts can be further used to perform certain photocatalytic reactions depending on their thermodynamic viability. Titanium dioxide (TiO_2) was extensively used for photocatalytic hydrogen production due to its feasible conduction band potential, stability, and cost-effectiveness [32]. However, serious drawbacks still persist in TiO_2 disabling its potential utilization. Among the noted ones, the fast recombination of charge carriers and its operational capability in UV light strictly inhabits its potential utilization. People have suggested numerous strategies for improving the photocatalytic response of TiO_2 , such as metal doping, structural modification, and heterojunction formation with low band gap materials. During recent years the heterojunction formation with carbon and Cu-based materials gained importance in photocatalysis [33–35]. These materials enable TiO_2 to operate in visible light and provide an additional co-catalytic effect for an effective photocatalytic water-splitting reaction. The heterojunction formation leads to the development of a Schottky barrier which enables the easy inter-junctional transfer of electrons, thus decreasing the rate of recombination. Copper, in particular, is widely utilized as a dopant in TiO_2 in efforts to enhance photocatalytic performance. Relative to pristine materials, Cu doped titanium dioxide (Cu-TiO_2) is commonly reported to exhibit improved electron-hole separation with photoexcitation. Apart from that, keeping an eye

on energy demand in the world, hydrogen (H_2) will be the fuel of the future, and stage by stage, it will replace all current fossil fuels [36–39]. In this regard, during the current study, the $FCs@Cu^{2+}$ composite was immobilized on commercially available TiO_2 to produce a ternary $FCs@CuO@TiO_2$ heterojunction, which was further utilized for the photocatalytic hydrogen production from water. The P25 (TiO_2) was selected for this study as it is a commercially available, recognized, and easily available form of TiO_2 . The interesting part of this study is the synthesis of FCs, which is helpful for the sensitization of TiO_2 in visible light. This article presents a three-stage process: first, to convert LDPE precursor to FCs; second, using FCs as sensors ($FCs@Cu^{2+}$) for Cu^{2+} ions detection; and third, to fabricate $FCs@CuO@TiO_2$ composite as photocatalyst for hydrogen production via water splitting.

2. Experimental

2.1. Materials

Low-density polyethylene (LDPE, 99%), copper acetate (98%), and titanium dioxide (TiO_2 -P25) were purchased from Alfa Aesar, Ward Hill, MA, USA. Sulphuric acid (H_2SO_4 , 65 wt%), nitric acid (HNO_3 , 28 wt%), and ammonia (NH_3 , 28 wt%) were purchased from Sigma Aldrich, St. Louis, MO, USA. All the chemicals purchased were utilized without any supplementary purification, and deionized water (DI) was utilized during the experiment.

2.2. Synthesis of FCs and $FCs@CuO@TiO_2$ Composite

For the synthesis of FCs, 2 g of LDPE powder (commercially available) was added into the mixture of H_2SO_4 (10 mL), and HNO_3 (2.0 mL) and the suspension was sonicated for 1 h. The suspended mixture was firmly shifted to a Teflon-lined autoclave and heated at $180\text{ }^\circ\text{C}$ for 10 h. The final mixture was kept at room temperature to cool down and diluted with ammonia to adjust the pH to neutral behavior.

The FCs were used for the detection of Cu^{2+} ions. After the detection procedure, the $FCs@Cu^{2+}$ interface was formed, which was kept for the synthesis of ternary composite ($FCs@CuO@TiO_2$).

The $FCs@CuO@TiO_2$ composite was prepared by the wet impregnation method. A suspension of commercial TiO_2 , P25 (0.5 g) in water (20 mL) was stirred at room temperature and then 1.0 mL of $FCs@Cu^{2+}$ (1:1 v/v) solution was tapped dropwise. For achieving homogeneity, the mixture was stirred continuously for 4 h at room temperature to make a homogenous solution. The samples were washed with DI water through centrifugation and kept for drying at $80\text{ }^\circ\text{C}$ for 5 h. The as-prepared photocatalyst was abbreviated as $FCs@CuO@TiO_2$.

2.3. Characterization Techniques

The UV–vis absorption spectra were recorded at room temperature with Perkin Elmer spectrophotometer UV-2600. PL excitation spectra and excitation-dependent emission spectra were recorded using Perkin Elmer Fluorescence Spectrophotometer LS55. The lifetime decay was recorded on a fluorometer, Fluoro Max-4, an excitation wavelength of 390 nm was chosen, and emission was recorded at $\lambda_{em} = 410\text{ nm}$ to 680 nm. The XRD data were recorded on an X-ray powder diffractometer, Rigaku MiniFlex, among $Cu\ K\alpha$ radiation ($\lambda = 1541\text{ \AA}$, 30 kV, 10 mA). The morphological structure for the samples was examined by transmission electron microscopy (TEM) and scanning electron microscopy (SEM). The SEM measurement was examined by using a field-emission scanning electron microscope (FESEM, JEOL JSM 7100 TTLS) stimulated with an energy dispersive X-ray spectrometer (EDXS, Oxford X-Max80). For the TEM analysis, the samples were initially suspended in ethanol then dropped upon copper-grid-supported lacey carbon film. The TEM study was achieved with a field-emission electron microscope (JEOL JEM 2100UHR) operational at 200 kV and fortified by an energy-dispersive X-ray spectroscopy detector, EDXS (Oxford X-Max80T). The functional groups for the samples were investigated by IR spectrophotometer (IR-ATR) Perkin Elmer Spectrum 100 equipped with PIKE Gladi ATR. Raman spectra were obtained using a Raman spectrometer (RENISHAW, Wotton-

under-Edge, UK). The microstructural characterization designed to evaluate the specific surface area, the total pore volume, and the pore size of the samples were evaluated by N_2 physisorption at $-196\text{ }^\circ\text{C}$ with a Micromeritics ASAP 2010 instrument. Samples were degassed at $150\text{ }^\circ\text{C}$, and the specific surface area (SSA) was calculated in the relative pressure (p/p_0) range between 0.05 and 0.30 by applying the Brunauer–Emmett–Teller (BET) multipoint method. Electrochemical characteristics (ζ -potential) for the samples diluted with water were examined as per function of the suspension pH via a Zeta PALS instrument (Brookhaven Instruments Corporation, New York, NY, USA). Relatively, the pH of the aqueous solution was regulated with dilute hydrochloric acid and sodium hydroxide.

2.4. Fluorescence Sensing of Cu^{2+} Ions

For the sensing experiments, $10\text{ }\mu\text{L}$ of the standard solution of Cu^{2+} was solubilized with 1 mL of FCs in a quartz cuvette. The PL spectra were noted instantly after an aliquot of the standard solution of metal ions was mixed. Each test was repeated at least three times to obtain concordant values. All the experiments, if otherwise indicated, were excited at $\lambda_{\text{ex}} = 390\text{ nm}$ besides the associated emission wavelength was assayed from $\lambda_{\text{em}} = 410$ to 680 nm . The profile of the emission spectra was not altered with the accumulation of the standard solutions of metal ions. After the detection procedure, the FCs@ Cu^{2+} solution was kept for the synthesis of ternary composite (FCs@CuO@TiO₂).

2.5. Photocatalytic and Photo Electrochemical System

The photocatalytic experiment for hydrogen production was carried out in a quartz photocatalytic reactor (100 mL capacity, Perfect light) under 1.5 AM solar radiation. In each photocatalytic reaction, 10 mg of catalyst was suspended into a 40 mL water:methanol mixture ($4:1\text{ }v/v$) with continuous stirring. The experiment was carried out under vacuum, and before the start, the reaction mixture was purged with Ar for 20 min . The temperature was adjusted at $25\text{ }^\circ\text{C}$, via the continuous water-cooling system. The hydrogen produced during the reaction was measured using an online Thermal Conductivity detector-based Gas Chromatograph (GC979011, China made) installed with a 13 X molecular sieve column. The detector temperature was set at $180\text{ }^\circ\text{C}$, while for the column and injector, the temperature was set at $30\text{ }^\circ\text{C}$ and $100\text{ }^\circ\text{C}$, respectively. The sampling frequency of the autosampler was set at 60 min .

For the photoelectrochemical (PEC) study, the photocatalytic material, FCs@CuO@TiO₂ (10 mg) dispersed in 10 mL of EtOH containing $10\text{ }\mu\text{L}$ Nafion binder was ultrasonicated for 30 min . At the same time, cleaned FTO ($2 \times 2\text{ cm}$) was placed in a Petri plate with its conductive surface positioned upwards. The FCs@CuO@TiO₂ dispersion was added to these Petri plates dipping the FTO glass completely. After evaporating the EtOH at $80\text{ }^\circ\text{C}$ for 12 h , a thin film of photocatalytic material was formed, which was further calcined at $180\text{ }^\circ\text{C}$ for 2 h before use.

The PEC activity of the sample electrodes (thin film on FTO glass) was determined by using a standard three-electrode cell with saturated Ag/AgCl (3 M , KCl) acting as a reference electrode and platinum wire as the counter electrode. The light source used was 1.5 A.M simulated solar light radiance ($100\text{ mW}/\text{cm}^2$) by a Xe lamp (300 W); the reaction analysis was conducted in 0.1 M of sodium sulfate solution ($\text{pH} \approx 6.7$) as an electrolyte. The LSV analysis was performed with a scan rate of $10\text{ mV}/\text{s}$ and at different applied potentials from -1.0 to 1.0 V vs. Ag/AgCl. Additionally, the potential of the working electrode (vs. Ag/AgCl) can be switched with the reversible hydrogen electrode (RHE) using the Nernst equation:

$$E_{\text{RHE}} = E_{\text{Ag/AgCl}} + 0.0591\text{pH} + 0.19742$$

3. Results and Discussion

3.1. Characterization of FCs

Hydrothermal treatment has been recognized as an effective method to synthesize active carbonaceous materials with photoluminescent characteristics from numerous renewable materials such as natural saccharides [40,41]. Inspired by these reports, we used LDPE as a precursor for the synthesis of FCs.

During synthesis, it was observed that the reaction initiated with the degradation of LDPE to succinic acid and then completely degraded into FC nanosheets. The formation of succinic acid was confirmed at the halfway stage of the reaction by ammonia. Succinic acid produces a yellow coloration during the initial half of the reaction, and after the introduction of ammonia, it changes to the greenish fluorescent liquid. The UV-vis spectra of as-synthesized FCs showed an absorption band at 300 nm (Figure 1a); this absorption band signifies the $n \rightarrow \pi^*$ transition of electrons in the orbital due to C=O binding.

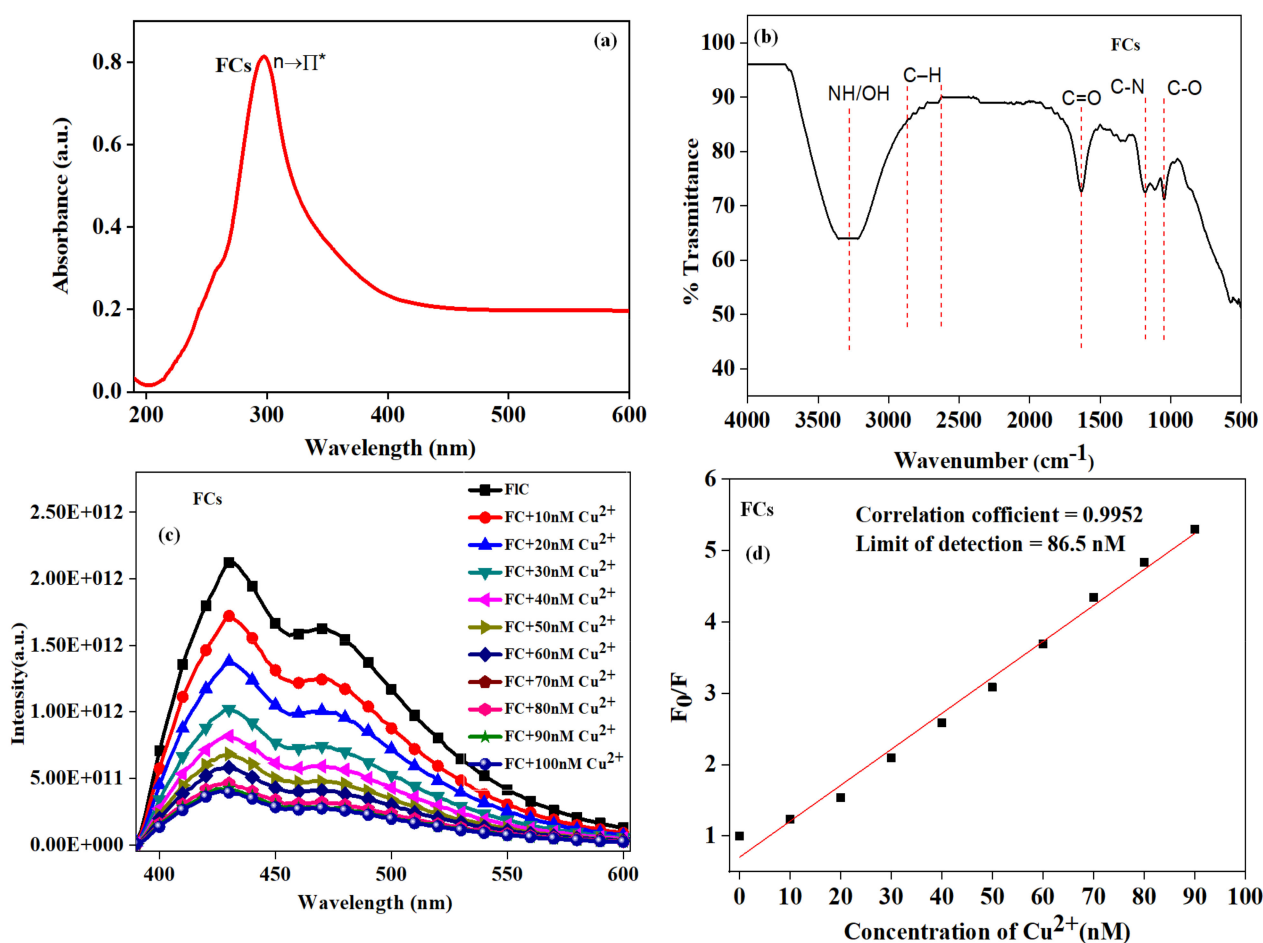


Figure 1. (a) UV-vis absorbance, (b) FTIR spectra for FCs (c) PL intensity suppression of FCs in the presence of different concentrations of Cu²⁺ ions (d) The relative fluorescence intensity of FCs to the concentration of Cu²⁺ ions: The linear fitting to the relationship of F/F_0 versus Cu²⁺ ions concentration from 10 to 90 nM.

The fluorescence spectrum of FCs is presented in Figure 1c; the emission spectrum of FCs depicts two significant emission peaks and wavelengths, 430 nm and 470 nm. It is very exceptional to observe two emission peaks for a fluorescence material; these electronic transitions arise due to the interorbital electronic transition from HOMO to LUMO of carbon material. Such phenomenon is also termed as stimulated emission, a double-

electron emission observed when the material undergoes recombination progression owing to photons by UV rays absorbed by the FCs.

The FTIR analysis shown in Figure 1b revealed a broad adsorption band from 3200–3400 cm^{-1} corresponding to OH/NH stretching, broadening of the peak is due to a hydroxyl group and overlapping of the OH/NH groups. The other distinctive peaks at 2800–2500 cm^{-1} , 1640 cm^{-1} , 1180 cm^{-1} , and 1040 cm^{-1} confirm the existence of C–H, C=O, C–N, and C–O groups agreeing well with UV-visible absorption results. The surface charge of the FCs at pH = 7 was recorded as -14.84 mV by zeta potential analysis. The negative surface charge of FCs leads to the formation of fractions; such kind of fractions is crucial to achieving an admirable dispersion of FCs in an aqueous-based solvent. The zeta-potential and FTIR outcome recognized the surface of as-synthesized FCs as intrinsically negatively charged fractions, which are assumed to be vital for their long-term water dispersion.

3.2. Sensing Application of FCs towards Cu^{2+} Ions

Considering the brilliant fluorescence photostability and plentiful surface-functionalized sets, we attempted to utilize the as-synthesized FCs as a sensing probe aimed at Cu^{2+} ions. The FCs depict maximum emission when excited at 370 nm, and drastic change was observed in the fluorescence intensity after the addition of Cu^{2+} ions, as shown in Figure 1c. A sequence of concentrations of Cu^{2+} was added to the FCs detection solution for analyzing the analytic implementation of the primed fluorescent probe. As demonstrated in Figure 1c, the fluorescence intensity declined via both peaks after the Cu^{2+} concentrations were amplified. A fine linear relationship among fluorescence quenched values (F_0/F with Cu^{2+} concentration) within the values of 10 to 100 nM is achieved. The quenching percentage started with 19.3% for 10 nM Cu^{2+} addition, and it lasted for 81.1% with 90 nM Cu^{2+} ; later, no further quenching was observed. The following Stern–Volmer equation was used to understand the quenching effect quantitatively.

$$\Delta F_0/F = K_{SV}[Q] + 1,$$

Here F and F_0 stand for the fluorescence intensity of FCs in the presence and absence of the Cu^{2+} ions; individually, $[Q]$ stands for concentration of Cu^{2+} ions (100 nM) and K_{SV} for Stern–Volmer quenching constant. The fluorescence intensity of the FCs versus Cu^{2+} ions showed brilliant analytical capability in sensing Cu^{2+} through an extensive sensing range. The good linearity is shown in the range of 30 nM–90 nM with a correlation coefficient R^2 of 0.9952, as shown in Figure 1d. Notably, the limit of detection (LOD) was evaluated to be 86.5 nM by the equation $3\sigma/k$ (where σ stands for the standard deviation of the signals from FCs and k for the slope of the calibration curve), plus the evaluated LOD is considerably lesser compared to other formerly reported fluorescence probes derived from waste. Fluorescent carbon possesses a variety of functional groups and optical properties, which could bind targets through different mechanisms such as the inner filter effect, aggregation-induced emission quenching, or electron transfer. In this work, the possible mechanism was investigated by the zeta potential. The zeta potential value is found to be increased from -14.84 mV to 6.97 mV after the addition of Cu ions into FCs. This suggests that successful quenching results are due to the electrostatic effect between FCs and Cu ions, which can also be attributed to the chelation of Cu^{2+} ions by FCs via the oxygen functional group present on the surface [41,42].

In order to test the selectivity of the FCs, quenching ability was performed with Cu^{2+} , Fe^{2+} , Co^{2+} , and Pb^{2+} metal ions (Figure S1). The fluorescence intensity of FCs decreased with the addition of metal ions, but with Cu^{2+} and Fe^{2+} , a significant change was observed. When competing Cu^{2+} with Fe^{2+} , Cu^{2+} won because of more drastic fluorescence quenching. Therefore, this FCs sensing system was proved to be specific for Cu^{2+} ions.

The quantum yield (QY) of FCs was calculated to be ~35.6%, investigated by comparing the integrated intensities (excited at 370 nm) and the absorbance value of FCs at 370 nm with reference quinine sulfate (QS) in 0.01 M H₂SO₄ (QY = 54%)

$$QY_S = QY_R \times \frac{\eta_R I_S}{\eta_S I_R} \times \frac{A_S}{A_R}$$

where QY, I, A, and η are assigned to QY, integrated PL intensity, absorbance values, and refractive index, respectively. The subscript R and S refer to reference and sample.

3.3. Morphological Characterization of FCs and FCs@CuO@TiO₂ Composite

The surface morphology of FCs was obtained by TEM images, as represented in Figure 2. The analysis revealed two types of FCs with different morphologies: 0.5 μ m large sheet-like particles (Figure 2a) and 0.5–1 μ m large elongated structures (Figure 2b). The TEM analysis also revealed that both types of particles are amorphous in nature. The acidic mixture and hydrothermal treatment are important for the hydrolysis and oxidative degradation of the LDPE polymer. Apart from this, the production of two different shapes indicates that the mixture of acids plays a greater role in defining the morphology of FCs. The two different shapes produced are the very thin sheet-like 2D morphology with irregular geometry and elongated particles.

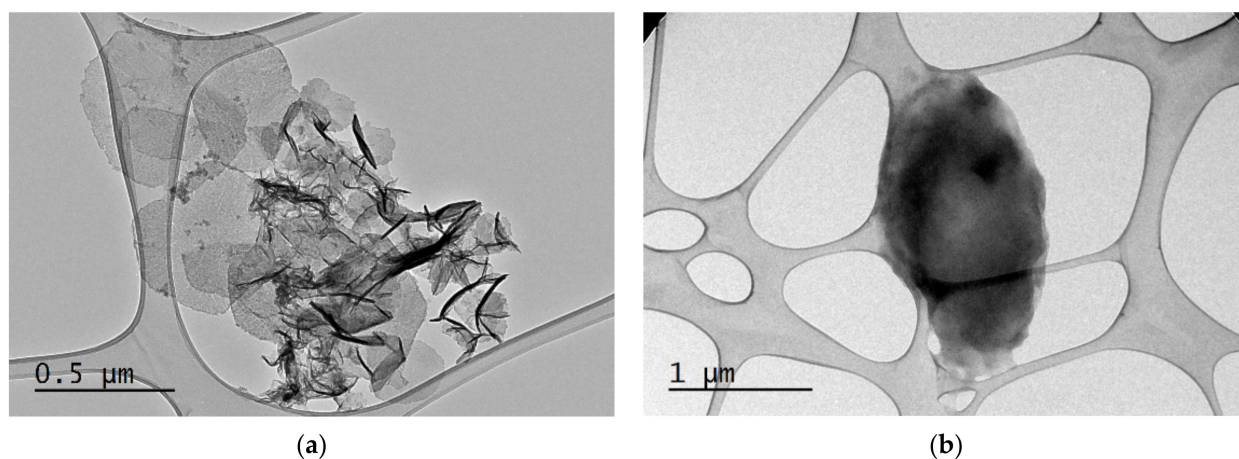


Figure 2. TEM image of sheet-like (a) and elongated (b) particles resulted from hydrothermal treatment of low-density polyethylene (LDPE).

The functionality of TiO₂ nanomaterials for diverse applications is entirely dependent on its crystal phase. The anatase phase of TiO₂ is preferred for photocatalytic applications, while the rutile phase is ideal for applications in pigments [31]. Thus, after the sensing application, the remaining solution (FCs@Cu²⁺) was mixed with TiO₂, and after drying, the FCs@CuO@TiO₂ composite was formed, which was confirmed by XRD (Figure 3a). The typical diffraction pattern of the composite FCs@CuO@TiO₂ showed the characteristics peaks of 80% anatase (JCPDS card 21-1272) and 20% rutile (JCPDS card 21-1276), TiO₂. The main focus was on the heterojunction development between TiO₂ and CuO; as evidenced by the XRD results, there is no major diffraction peak of the Rutile form of TiO₂. Therefore, the heterojunction is expected between anatase TiO₂ and CuO. Due to the lower content of CuO, a single characteristic peak was observed at 35.5°, which corresponds to (002) lattice planes of tenorite, and no additional crystalline forms of copper oxide (CuO) were observed. The X-ray diffraction pattern of FCs@CuO@TiO₂ almost coincided with that of pure TiO₂, thus suggesting that CuO and carbon are well dispersed on the TiO₂ surface. Raman spectroscopy was employed to characterize the structure of the FCs@CuO@TiO₂ further. In the spectrum as shown in Figure 3b, the sharp peaks at 145 cm⁻¹, 400 cm⁻¹, 520 cm⁻¹, and 640 cm⁻¹ are associated with anatase TiO₂, one small broad peak at 1140 cm⁻¹ is ascribed

to CuO and two strong bands at around 1344 cm^{-1} (D band), and 1579 cm^{-1} (G band) corresponds to the FCs.

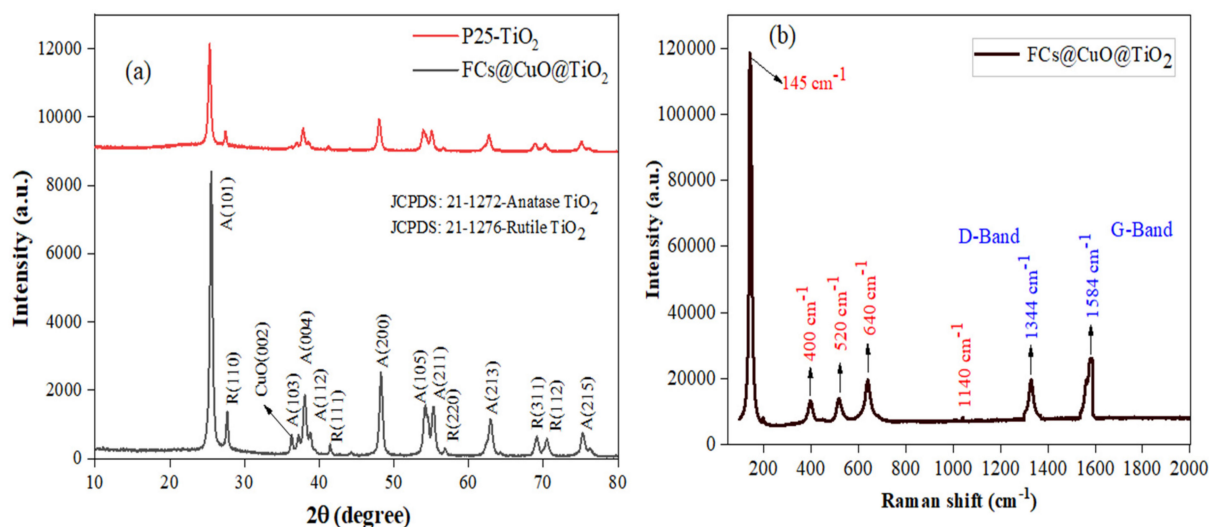


Figure 3. (a) Powder XRD pattern (b) Raman spectrum of FCs@CuO@TiO₂.

The formulation of ternary composite FCs@CuO@TiO₂ was also studied by TEM and HR-TEM. The TEM analysis revealed (Figure 4a,b) that the ternary mixture is a polycrystalline system made up of two types of particles, larger 10 nm–20 nm square-like and small 5 nm spherical nanoparticles embedded in the network of FCs. The square-shaped particles were anatase polymorph of TiO₂ in tetragonal geometry possessing (101) as a major plane with the inter-planar distance of 0.32 nm, which is in consonance with HRTEM results (Figure 3b). Furthermore, Figure 4c shows the HRTEM image of the 5 nm spherical particle deposited on TiO₂. The corresponding FFT pattern of this particle reveals the formation of CuO, and the pattern was indexed according to its monoclinic structure along [04-2] direction (Figure 4d). Moreover, a precise interfacial contact was observed between CuO [04-2] and TiO₂ (101), which is beneficial for interstate electron transfer. Moreover, FCs@CuO@TiO₂ was further verified by EDS analysis for the confirmation of the atomic ratio of the FCs and CuO, which is expected to be ~5 atomic% (Figure S2)

The surface area and porosity of the FCs@CuO@TiO₂ were investigated by using nitrogen adsorption and desorption isotherms (Figures S3 and S4). The isotherms are typical type IV-like with a type H2 hysteric loop; the plot of the pore size distribution was determined by using the Barrett–Joyner–Halenda (BJH) method from the desorption branch of the isotherm. As reported for commercially available, the specific surface area of P25-TiO₂ is $54\text{ m}^2/\text{g}$; for FCs@CuO@TiO₂, it is almost similar (57.94%). However, we see little increase in the pore diameter, from 16 nm (P25-TiO₂) to 31.07 for FCs@CuO@TiO₂, due to the accumulation of CuO particles into the pores of TiO₂.

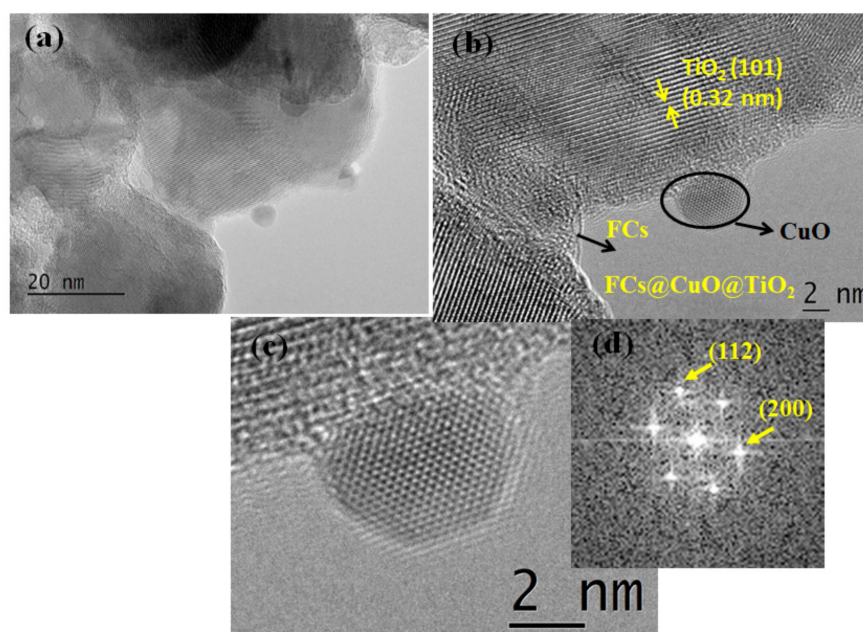


Figure 4. (a,b) TEM image of FCs@CuO@TiO₂ composite (c) HRTEM image of 5 nm particle attached to the TiO₂ particle with corresponding FFT (d) The FFT pattern was indexed according to the monotonic structure of CuO along [04-2].

3.4. Photocatalytic Hydrogen Production via Water Splitting

After the sensing application, the remaining solution (FCs@Cu²⁺) was mixed with TiO₂ to make FCs@CuO@TiO₂ composite, and its photocatalytic efficiency was analyzed for hydrogen production from water.

Controlled experiments in the absence of either photocatalyst or light irradiation revealed a negligible hydrogen production indicating the major role of the photocatalyst in the process. In order to recognize the specific role of individual components (FCs, CuO, and TiO₂) for the projected photocatalytic activity, these individual photocatalysts were put on trial with similar experimental conditions for the H₂ evolution. Figure 5 displays the rate of H₂ produced as the function of time using the FCs, CuO, Cu²⁺@TiO₂, and FCs@CuO@TiO₂ samples as photocatalysts. The H₂ evolution rate of FCs@CuO@TiO₂ was 1800 mmolg⁻¹ which is 9 times that of FCs, 5 times than Cu alone, and 2.5 times that of FCs@CuO. Here, FCs and CuO showed a synergistic part for the suppression of their combination of the photogenerated carriers in the TiO₂ phase. Furthermore, the lifetime of the final composite was also compared with the value of commercial P25-TiO₂, which is already reported. It was observed that the lifetime of ternary composite is higher than both P25-TiO₂ and FCs [43–45]. The photocatalytic efficiency of FCs@CuO@TiO₂ is also compared with the reported similar articles (Table S2), which shows better results of the present photocatalyst.

Significantly, recyclability, durability, and efficiency are key features for an efficient photocatalyst. By evaluating the above-mentioned features, the recyclability trials were performed by relinquishing the produced gases with systematic intervals for the subsequent cycles, and the outcomes are presented in Figure 6a; a persistent H₂ evolution rate was detected for all three sets. After the third cycle, we observed that the mass of photocatalyst after filtration decreased from 10 mg to 8 mg, which is the reason for decreased photocatalytic activity. In order to examine more, we performed an EDS analysis of the photocatalyst after three consecutive cycles (Figure S5). Through EDS, we observe that the ratio of CuO was reduced by 0.5%, which is the reason behind the decreased photocatalysis after three cycles. The obtained outcomes show that the FCs@CuO@TiO₂ photocatalyst can be effectually reused for several cycles without degrading its photocatalytic activity, which visibly exemplified its upright stability. The higher photocatalytic response of FCs@CuO@TiO₂ is also credited to its lower band gap value corresponding to 2.44 eV (Figure 6b) and better

charge separation observed by fluorescence decay measurement (Figure 6d). The lifetime of charge carriers in FCs@CuO@TiO₂ is 10.5 ns, which is comparatively higher than FCs and commercial P25-TiO₂.

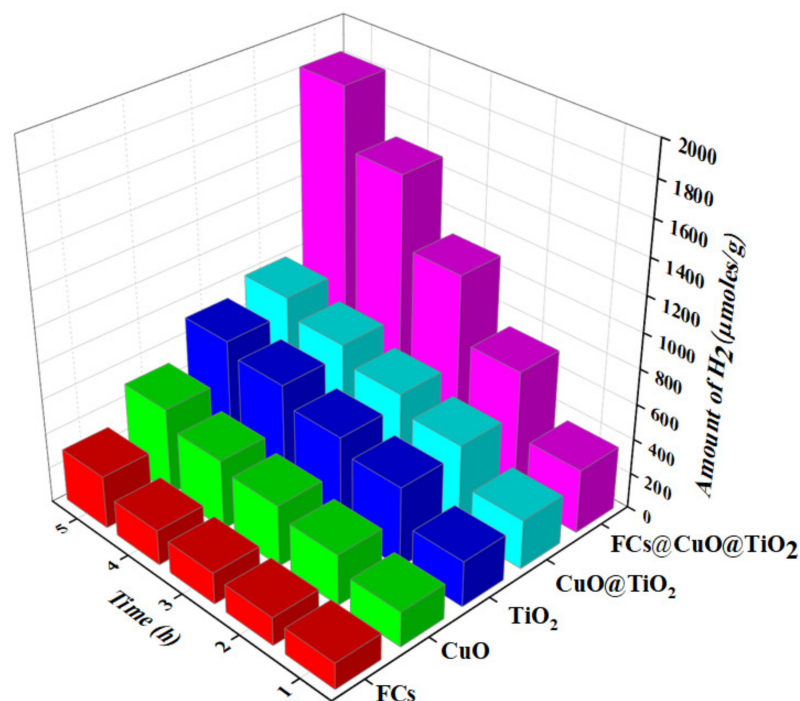


Figure 5. Comparison of the photocatalytic activity of FCs, CuO, Cu²⁺@TiO₂, and FCs@CuO@TiO₂ for the H₂-production from water: methanol aqueous solution under 1.5 M solar irradiation.

3.5. PEC Water Splitting Performance

In order to use the FCs@CuO@TiO₂ photoanode for PEC water splitting in solution, a thin film was prepared by the drop-casting technique. As shown in Figure 7a, the linear sweep voltammetry (LSV) curves display the photoelectrochemical (PEC) characteristics of the as-synthesized samples. The samples showed no results in the dark, while when under simulated solar light, the transient photocurrent density of pristine TiO₂ reached 0.6 mA/cm² under an applied bias of 1.0 V (vs. RHE), pure comparative FCs nearly shows negligible PEC response. The photocurrent density of ternary FCs@CuO@TiO₂ composite showed a significant increase to about 2.40 mA/cm², measured at the same potential.

The stability of the FCs@CuO@TiO₂ was assessed by measuring the photocurrent–time (I–t) response. Notably, photocurrent density is almost zero with no illumination. As soon as illumination was switched on, photocurrent density reached 2.40 mA/cm². As depicted in Figure 7b, the photocurrent density of the FCs@CuO@TiO₂ electrode showed insignificant decay even after 1400 min of illumination, which reveals that FCs@CuO@TiO₂ has excellent stability for PEC water oxidation.

The STH efficiencies (η) of catalysts were intended by the equation

$$\eta = I(1.23 - V)/J_{\text{light}}$$

where I stands for the photocurrent density with measured bias, V stands for applied bias vs. RHE, and J_{light} stands for irradiance intensity of 100 mW/cm² (AM 1.5 G). We plotted the evaluated STH efficiency versus the function of applied bias as depicted in Figure 7c. The FCs@CuO@TiO₂ composite displays optimum conversion efficiency of nearly 0.95%, which is higher than pristine TiO₂ and FCs. Hydrogen evolution significantly improved the photoconversion efficiency of FCs@CuO@TiO₂ by dropping the current saturation potential and improving the higher photocurrent.

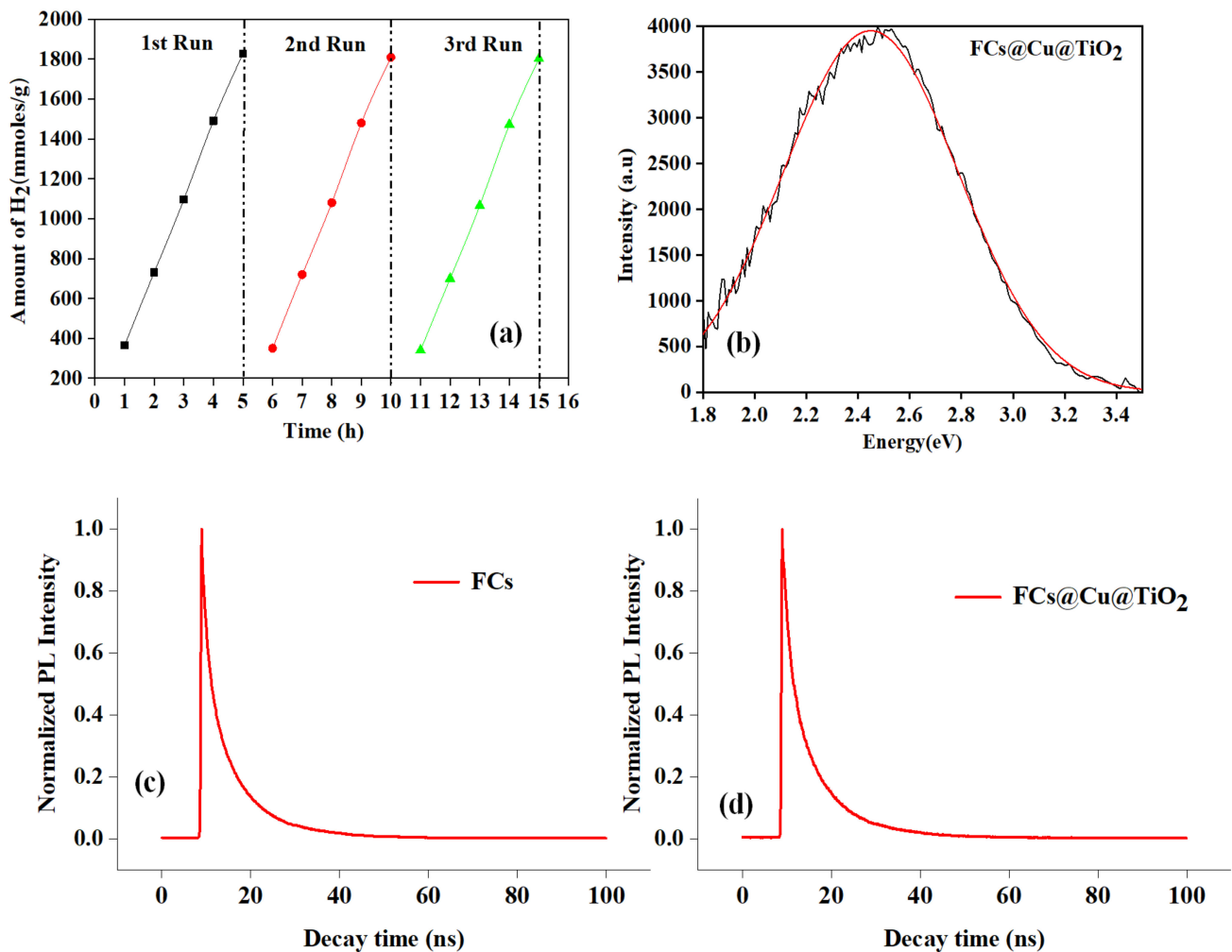


Figure 6. (a) Recycling measurements of photocatalytic hydrogen generation over FCs@CuO@TiO₂; (b) CL spectra collected for FCs@CuO@TiO₂; (c,d) Fluorescence decay curves of FCs and FCs@CuO@TiO₂ with excitation of 486 nm.

An electrochemical impedance spectrum (EIS) was recorded to recognize the charge transfer route at the interface of photoelectrode and electrolyte. From Figure 7d, electrochemical impedance spectra display that the pristine P25-TiO₂ possess higher resistance compared to FCs@CuO@TiO₂, which indicates that the support of CuO has successfully promoted the separation of electron and hole, which also permits high-speed electron transference for water splitting.

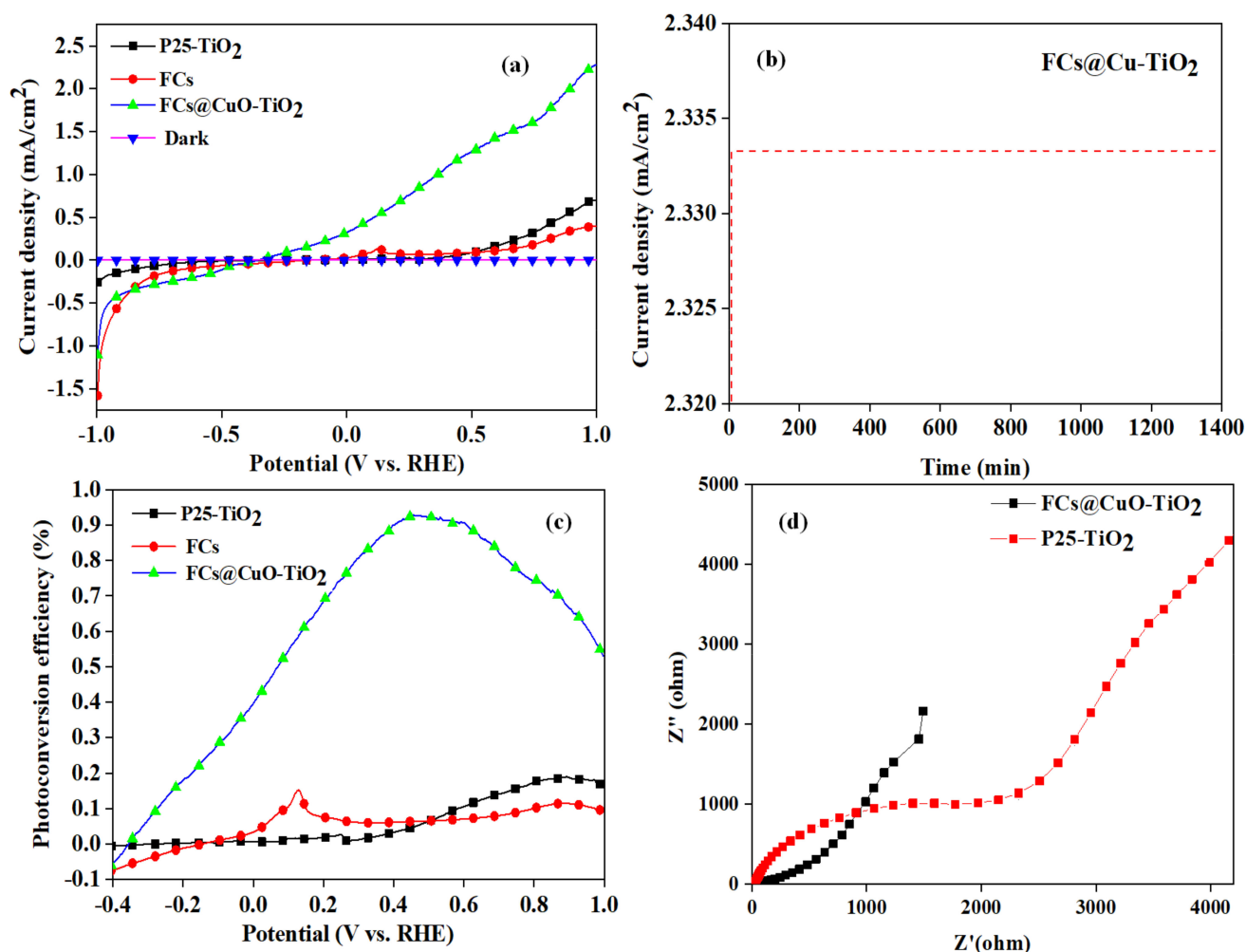


Figure 7. (a) Photocurrent density vs. potential curves for the FCs@CuO@TiO₂, FCs, P25-TiO₂, and in the dark; (b) Chronoamperometry (I-t) of FCs@CuO@TiO₂ with a three-electrode system at 1.23 V_{RHE} for 1400 min; (c) Photoconversion efficiency as a function of applied potential; (d) EIS spectra of the FCs@CuO@TiO₂ and P25-TiO₂.

4. Plausible Mechanism

The ternary composite was found as an exceptional photocatalyst to produce H₂ under 1.5 AM solar stimulation. Previous reports suggested that the conduction band (CB) of CuO is more positive hence not feasible for H₂ production [46–48]. However, in the FC's@CuO@TiO₂ ternary composite, the size of CuO reaches below 10 nm, which is responsible for the elevation of CB level due to quantum effect, which decreases the recombination rate and thus making the system suitable for H₂ evolution. Another novel aspect of the FCs@CuO@TiO₂ is the highest fluorescence carbon sheets embedding CuO@TiO₂, which provides a full spectrum for the composite by reaching the bandgap up to 2.44 eV as analyzed by CL analysis (Figure 6c).

The plausible mechanism of operation of FCs@CuO@TiO₂ is shown in Scheme 1. Under 1.5 AM stimulation, all three components are excited. However, due to the low percentage of UV-region at 1.5 AM, the excitation of TiO₂ is minimized. The excitation due to FCs is worth to be noted due to its fluorescence nature. Due to visible light activation, both FCs and CuO are activated, followed by electronic excitations. The e⁻ from FCs was injected into the CB of TiO₂, followed by its crossover to CB of CuO due to its more positive potential vs. NHE. The conduction band value of CuO is not enough negative to drive the H₂ evolution reaction. However, once a heterojunction or interfacial contact is established between TiO₂ (E_g = 3.2 eV) and CuO (E_g = 2.2 eV), both are excited under

UV and visible light, respectively [49–53]. Since the conduction band of TiO_2 is more negative than CuO , after the fermi level equilibration of the system, the band bending occurs, causing the fermi energy level of CuO to increase, thus providing it a driving force for hydrogen evolution reaction. On the surface of CuO , the electrons are consumed by H^+ ions, thus generating the H_2 gas, while the holes generated during the process are consumed by sacrificial agent (CH_3OH) in a half-reaction. The ternary composite is responsible for enhancing the lifetime of the exciton (e^- and h^+), as shown in Figure 4c,d. To further examine the transfer mechanism of the holes and electrons in the ternary composite and to determine the fluorescence lifetimes of FCs and FCs@CuO@TiO_2 , we utilized the transient fluorescence spectroscopy method. Figure 4b,c depicts the exponential behavior of fluorescence intensities that could be fitted with the two radiative lifetimes: The different lifespan fluctuations are shown in Table 1. The photoluminescence decay curves were fitted to a two-exponential function:

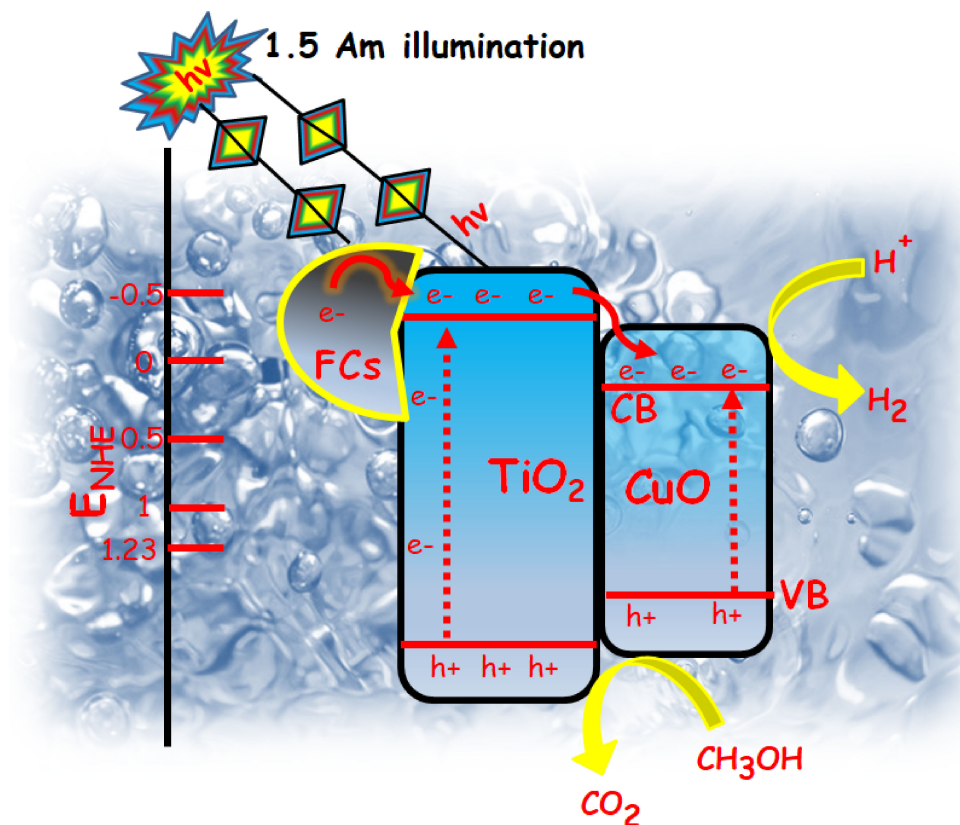
$$I(t) = A + B_1 \cdot e^{(-t/\tau_1)} + B_2 \cdot e^{(-t/\tau_2)},$$

R_i is the relative ratio factor which is calculated by $R_i = B_i / (\sum_{i=1}^2 B_i)$.

The average life could be examined with the theoretical formula shown in Table 1:

$$\tau_{average} = \sum_{i=1}^2 R_i \cdot \tau_i.$$

The average lifetimes of FCs and FCs@CuO@TiO_2 were calculated as 9.61 ns and 10.64 ns individually via the above equation. For the photocatalyst, usually, the extension of the lifetime infers that the excited electrons or holes are expected to be tangled during the entire photocatalytic reaction, which was the reason for FCs@CuO@TiO_2 showing a remarkable photocatalytic activity for H_2 production.



Scheme 1. Plausible illustration of the charge separation and transport mechanism in the FCs@CuO@TiO_2 system.

Table 1. The comparison chart of the average lifetime ($\tau_{average}$) of different catalysts.

Catalyst	λEm (nm)	τ_1	τ_2	B_1	B_2	R_1	R_2	A	χ^2	τ_{1avg} (ns)	τ_{2avg} (ns)	$\tau_{average}$
FCs	486	1.18	8	0.17	0.15	1.15	1.032353	525.2	22.31	1.357	8.258823529	9.61582352
FCs@CuO@TiO ₂	486	1.38	8.21	0.17	0.16	1.16	1.101176	1690	60.73	1.6008	9.040658824	10.64145882

5. Conclusions

The current study demonstrates a novel synchronized strategy towards tackling the most important global issues, i.e., waste utilization, water treatment, and hydrogen production. The work highlights a green, cheap, and simple approach to synthesizing fluorescence carbon (FC) by hydrothermal treatment of commercial LDPE (most commonly used plastic source) without any intricate post-treatment. The as-prepared FCs were found to exhibit high fluorescence properties stimulatingly with two emission bands, thus applied for the sensing of Cu ions in aqueous solutions. The sensing results were quite successful with the LOD of 86.5 nM, signifying their prospective application for the determination of Cu²⁺ ions in industrial wastewater. Afterward, in a smart way, the waste sensed solution FC@CuO was doped with TiO₂ to fabricate FCs@CuO@TiO₂ composite. Remarkably the ternary composite was found to exhibit good photocatalytic efficiency proved on the basis of the evolution of H₂ via water splitting experiment. The H₂ evolution rate of FCs@CuO@TiO₂ was observed to be 9 times higher than that of FCs, 5 times than Cu alone, and 2.5 times that of FCs@Cu²⁺. Moreover, the optimized FCs@CuO@TiO₂ composite exhibits an STH efficiency of 0.95%, which is the best value for TiO₂ materials. This study opens new avenues to utilize real waste plastic sources to treat wastewater and produce energy simultaneously.

Supplementary Materials: The following supporting information can be downloaded at: <https://www.mdpi.com/article/10.3390/en15051734/s1>, Figure S1: Selectivity of the FCs toward different metal ions. Figure S2: EDS analysis of FCs@CuO@TiO₂. Figure S3: Nitrogen adsorption-desorption isotherms of FCs@CuO@TiO₂. Figure S4: BJH plot of FCs@CuO@TiO₂. Figure S5: EDS analysis of FCs@CuO@TiO₂ after 3 cycles. Table S1: Comparative textural properties of FCs@CuO@TiO₂ with P25-TiO₂. Table S2: Comparison table for photocatalytic efficiency of FCs@CuO@TiO₂ with reported articles.

Author Contributions: (1) A.M.: Responsible for leading the project and writing the manuscript. (2) R.A.R.: Execution of photocatalytic hydrogen production study. (3) B.B.: Responsible for morphological characterization study, which includes SEM and TEM analysis. (4) S.G.: Responsible for Fluorescence characterization technique to study the sensing of metal ions. (5) M.F.: Execution of photocatalytic hydrogen production study. (6) M.V.: Guidance and financial support to execute the project and to technically correct the manuscript. All authors have read and agreed to the published version of the manuscript.

Funding: This research received no external funding.

Institutional Review Board Statement: Not applicable.

Informed Consent Statement: Not applicable.

Data Availability Statement: Not applicable.

Acknowledgments: For the financial support, the authors acknowledge Slovenian Research Agency (research core funding No. P2-0412). We also thank Thanveer Thanjudin and Uros Luin (University of Nova Gorica, Slovenia) for the help in characterizations.

Conflicts of Interest: The authors report no declarations of interest.

References

1. Beg, M.D.H.; Kormin, S.; Bijarimi, M.; Zaman, H.U. Preparation and Characterization of Low-Density Polyethylene/Thermoplastic Starch Composites. *Adv. Polym. Technol.* **2015**, *35*, 21521–21529. [[CrossRef](#)]
2. Ugoeze, K.C.; Amogu, E.O.; Oluigbo, K.E.; Nwachukwu, N. Environmental and public health impacts of plastic wastes due to healthcare and food products packages: A Review. *J. Environ. Public Health* **2021**, *5*, 1–31.
3. Siegle, L. *Turning the Tide on Plastic: How Humanity (and You) Can Make Our Globe Clean Again*; Hachette: New York, NY, USA, 2018.
4. Zhuo, C.; Levendis, Y.A. Upcycling waste plastics into carbon nanomaterials: A review. *J. Appl. Polym. Sci.* **2014**, *131*, 39931. [[CrossRef](#)]
5. Sun, X.; Wang, Y.; Lei, Y. Fluorescence based explosive detection: From mechanisms to sensory materials. *Chem. Soc. Rev.* **2015**, *44*, 8019–8061. [[CrossRef](#)] [[PubMed](#)]
6. Singh, J.; Kaur, S.; Lee, J.; Mehta, A.; Kumar, S.; Kim, K.-H.; Basu, S.; Rawat, M. Highly fluorescent carbon dots derived from *Mangifera indica* leaves for selective detection of metal ions. *Sci. Total Environ.* **2020**, *720*, 137604. [[CrossRef](#)] [[PubMed](#)]
7. Mehta, A.; Mishra, A.; Kainth, S.; Basu, S. Carbon quantum dots/TiO₂ nanocomposite for sensing of toxic metals and photodetoxification of dyes with kill waste by waste concept. *Mater. Des.* **2018**, *155*, 485–493. [[CrossRef](#)]
8. Ravi, S.; Vadukumpully, S. Sustainable carbon nanomaterials: Recent advances and its applications in energy and environmental remediation. *J. Environ. Chem. Eng.* **2016**, *4*, 835–856. [[CrossRef](#)]
9. Lim, S.Y.; Shen, W.; Gao, Z. Carbon quantum dots and their applications. *Chem. Soc. Rev.* **2015**, *44*, 362–381. [[CrossRef](#)]
10. Feng, Z.; Adolffson, K.H.; Xu, Y.; Fang, H.; Hakkarainen, M.; Wu, M. Carbon dot/polymer nanocomposites: From green synthesis to energy, environmental and biomedical applications. *Sustain. Mater. Technol.* **2021**, *29*, e00304. [[CrossRef](#)]
11. Zulfajri, M.; Sudewi, S.; Ismulyati, S.; Rasool, A.; Adlim, M.; Huang, G.G. Carbon Dot/Polymer Composites with Various Precursors and Their Sensing Applications: A Review. *Coatings* **2021**, *11*, 1100. [[CrossRef](#)]
12. Meseldžija, S.; Petrovic, J.; Onjia, A.; Volkov-Husovic, T.; Nestic, A.; Vukelic, N. Utilization of agro-industrial waste for removal of copper ions from aqueous solutions and mining-wastewater. *J. Ind. Eng. Chem.* **2019**, *75*, 246–252. [[CrossRef](#)]
13. Al-Saydeh, S.A.; El-Naas, M.H.; Zaidi, S.J. Copper removal from industrial wastewater: A comprehensive review. *J. Ind. Eng. Chem.* **2017**, *56*, 35–44. [[CrossRef](#)]
14. Kaur, N.; Mehta, A.; Mishra, A.; Chaudhary, S.; Rawat, M.; Basu, S. Amphiphilic carbon dots derived by cationic surfactant for selective and sensitive detection of metal ions. *Mater. Sci. Eng. C* **2019**, *95*, 72–77. [[CrossRef](#)] [[PubMed](#)]
15. Karimzadeh, A.; Hasanzadeh, M.; Shadjou, N.; de la Guardia, M. Optical bio (sensing) using nitrogen doped graphene quantum dots: Recent advances and future challenges. *Trends Anal. Chem.* **2018**, *108*, 110–121. [[CrossRef](#)]
16. Tajik, S.; Dourandish, Z.; Zhang, K.; Beitollahi, H.; Van Le, Q.; Jang, H.W.; Shokouhimehr, M. Carbon and graphene quantum dots: A review on syntheses, characterization, biological and sensing applications for neurotransmitter determination. *RSC Adv.* **2020**, *10*, 15406–15429. [[CrossRef](#)]
17. Tofighy, M.A.; Mohammadi, T. Divalent heavy metal ions removal from contaminated water using positively charged membrane prepared from a new carbon nanomaterial and HPEI. *Chem. Eng. J.* **2020**, *388*, 124192. [[CrossRef](#)]
18. Stern, B.R. Essentiality and toxicity in copper health risk assessment: Overview, update and regulatory considerations. *J. Toxicol. Environ. Health Part A* **2010**, *73*, 114–127. [[CrossRef](#)]
19. Jaishankar, M.; Tseten, T.; Anbalagan, N.; Mathew, B.B.; Beeregowda, K.N. Toxicity, mechanism and health effects of some heavy metals. *Interdiscip. Toxicol.* **2014**, *7*, 60–72. [[CrossRef](#)]
20. Arbabi, M.; Golshani, N. Removal of copper ions Cu(II) from industrial wastewater: A review of removal methods. *Int. J. Epidemiol. Res.* **2016**, *3*, 283–293.
21. Tchounwou, P.B.; Yedjou, C.G.; Patlolla, A.K.; Sutton, D.J. Heavy metal toxicity and the environment. *Mol. Clin. Environ. Toxicol.* **2012**, *101*, 133–164.
22. Aragay, G.; Pons, J.; Merkoçi, A. Recent Trends in Macro-, Micro-, and Nanomaterial-Based Tools and Strategies for Heavy-Metal Detection. *Chem. Rev.* **2011**, *111*, 3433–3458. [[CrossRef](#)] [[PubMed](#)]
23. Basabe-Desmonts, L.; Reinhoudt, D.N.; Crego-Calama, M. Design of fluorescent materials for chemical sensing. *Chem. Soc. Rev.* **2007**, *36*, 993–1017. [[CrossRef](#)] [[PubMed](#)]
24. Bansod, B.; Kumar, T.; Thakur, R.; Rana, S.; Singh, I. A review on various electrochemical techniques for heavy metal ions detection with different sensing platforms. *Biosens. Bioelectron.* **2017**, *94*, 443–455. [[CrossRef](#)]
25. Raj, S.K.; Yadav, V.; Bhadu, G.R.; Patidar, R.; Kumar, M.; Kulshrestha, V. Synthesis of highly fluorescent and water soluble graphene quantum dots for detection of heavy metal ions in aqueous media. *Environ. Sci. Pollut. Res.* **2021**, *28*, 46336–46342. [[CrossRef](#)]
26. Peveler, W.J.; Yazdani, M.; Rotello, V.M. Selectivity and specificity: Pros and cons in sensing. *ACS Sens.* **2016**, *1*, 1282–1285. [[CrossRef](#)] [[PubMed](#)]
27. World Health Organization. *Adverse Health Effects of Heavy Metals in Children (No. WHO/HSE/PHE/EPE/11.01.07)*; World Health Organization: Geneva, Switzerland, 2011; Available online: <https://apps.who.int/iris/bitstream/handle/10665/336875/WHO-HSE-PHE-EPE-11.01.07-eng.pdf> (accessed on 20 December 2021).
28. How to Sustain a World Population of 10 Billion People? Available online: <https://www.theworldcounts.com> (accessed on 20 December 2021).

29. Qadri, R.; Faiq, M.A. Freshwater pollution: Effects on aquatic life and human health. In *Fresh Water Pollution Dynamics and Remediation*; Springer: Singapore, 2020; pp. 15–26.
30. Gujre, N.; Mitra, S.; Soni, A.; Agnihotri, R.; Rangan, L.; Rene, E.R.; Sharma, M.P. Speciation, contamination, ecological and human health risks assessment of heavy metals in soils dumped with municipal solid wastes. *Chemosphere* **2021**, *262*, 128013. [CrossRef]
31. Fatima, B. Characterization and Treatment of Real Wastewater from an Electroplating Company by Raw Chitin. In *Recent Advancements in the Metallurgical Engineering and Electrodeposition*; IntechOpen: London, UK, 2020; p. 107. Available online: <https://www.intechopen.com/books/recent-advancements-in-the-metallurgical-engineering-and-electrodeposition/characterization-and-treatment-of-real-wastewater-from-an-electroplating-company-by-raw-chitin> (accessed on 20 December 2021).
32. Macwan, D.P.; Dave, P.N.; Chaturvedi, S. A review on nano-TiO₂ sol–gel type syntheses and its applications. *J. Mater. Sci.* **2011**, *46*, 3669–3686. [CrossRef]
33. Yang, Y.; Zhou, C.; Wang, W.; Xiong, W.; Zeng, G.; Huang, D.; Zhang, C.; Song, B.; Xue, W.; Li, X.; et al. Recent advances in application of transition metal phosphides for photocatalytic hydrogen production. *Chem. Eng. J.* **2021**, *405*, 126547. [CrossRef]
34. Yang, Y.; Li, X.; Zhou, C.; Xiong, W.; Zeng, G.; Huang, D.; Zhang, C.; Wang, W.; Song, B.; Tang, X.; et al. Recent advances in application of graphitic carbon nitride-based catalysts for degrading organic contaminants in water through advanced oxidation processes beyond photocatalysis: A critical review. *Water Res.* **2020**, *18*, 116200. [CrossRef]
35. Yang, Y.; Zeng, G.; Huang, D.; Zhang, C.; He, D.; Zhou, C.; Wang, W.; Xiong, W.; Song, B.; Yi, H.; et al. In Situ Grown Single-Atom Cobalt on Polymeric Carbon Nitride with Bidentate Ligand for Efficient Photocatalytic Degradation of Refractory Antibiotics. *Small* **2020**, *16*, e2001634. [CrossRef]
36. Zhou, Y.; Wang, Y.; Wang, Y.; Yu, H.; Zhang, R.; Li, J.; Zang, Z.; Li, X. MXene Ti₃C₂T_x-Derived Nitrogen-Functionalized Heterophase TiO₂ Homo Junctions for Room-Temperature Trace Ammonia Gas Sensing. *ACS Appl. Mater. Interfaces* **2021**, *13*, 56485–56497. [CrossRef] [PubMed]
37. Hosseini, S.E.; Wahid, M.A. Hydrogen from solar energy, a clean energy carrier from a sustainable source of energy. *Int. J. Energy Res.* **2020**, *44*, 4110–4131. [CrossRef]
38. Wang, Y.; Zhou, Y.; Wang, Y.; Zhang, R.; Li, J.; Li, X.; Zang, Z. Conductometric room temperature ammonia sensors based on titanium dioxide nanoparticles decorated thin black phosphorus nanosheets. *Sens. Actuators B Chem.* **2021**, *349*, 130770. [CrossRef]
39. Zhou, Y.; Li, X.; Wang, Y.; Tai, H.; Guo, Y. UV Illumination-enhanced molecular ammonia detection based on a ternary-reduced graphene oxide–titanium dioxide–Au composite film at room temperature. *Anal. Chem.* **2018**, *91*, 3311–3318. [CrossRef] [PubMed]
40. Kumari, A.; Kumar, A.; Sahu, S.K.; Kumar, S. Synthesis of green fluorescent carbon quantum dots using waste polyolefins residue for Cu²⁺ ion sensing and live cell imaging. *Sens. Actuators B Chem.* **2018**, *254*, 197–205. [CrossRef]
41. Li, C.; Zhang, C.; Gholizadeh, M.; Hu, X. Different reaction behaviours of light or heavy density polyethylene during the pyrolysis with biochar as the catalyst. *J. Hazard. Mater.* **2020**, *399*, 123075. [CrossRef]
42. Nicolae, S.A.; Au, H.; Modugno, P.; Luo, H.; Szego, A.E.; Qiao, M.; Li, L.; Yin, W.; Heeres, H.J.; Berge, N.; et al. Recent advances in hydrothermal carbonisation: From tailored carbon materials and biochemicals to applications and bioenergy. *Green Chem.* **2020**, *22*, 4747–4800. [CrossRef]
43. Li, Z.; Tian, B.; Zhen, W.; Wu, Y.; Lu, G. Inhibition of hydrogen and oxygen recombination using oxygen transfer reagent hemin chloride in Pt/TiO₂ dispersion for photocatalytic hydrogen generation. *Appl. Catal. B Environ.* **2017**, *203*, 408–415. [CrossRef]
44. Cheng, P.; Yang, Z.; Wang, H.; Cheng, W.; Chen, M.; Shangguan, W.; Ding, G. TiO₂–graphene nanocomposites for photocatalytic hydrogen production from splitting water. *Int. J. Hydrogen Energy* **2012**, *37*, 2224–2230. [CrossRef]
45. Charanpahari, A.; Umare, S.; Sasikala, R. Effect of Ce, N and S multi-doping on the photocatalytic activity of TiO₂. *Appl. Surf. Sci.* **2013**, *282*, 408–414. [CrossRef]
46. Hou, H.; Shang, M.; Gao, F.; Wang, L.; Liu, Q.; Zheng, J.; Yang, Z.; Yang, W. Highly efficient photocatalytic hydrogen evolution in ternary hybrid TiO₂/CuO/Cu thoroughly mesoporous nanofibers. *ACS Appl. Mater. Interfaces* **2016**, *8*, 20128–20137. [CrossRef] [PubMed]
47. Yang, Y.; Xu, D.; Wu, Q.; Diao, P. Cu₂O/CuO Bilayered Composite as a High-Efficiency Photocathode for Photoelectrochemical Hydrogen Evolution Reaction. *Sci. Rep.* **2016**, *6*, 35158. [CrossRef] [PubMed]
48. Mehta, A.; Pooja, D.; Thakur, A.; Basu, S. Enhanced photocatalytic water splitting by gold carbon dot core shell nanocatalyst under visible/sunlight. *N. J. Chem.* **2017**, *41*, 4573–4581. [CrossRef]
49. Khemthong, P.; Photai, P.; Grisdanurak, N. Structural properties of CuO/TiO₂ nanorod in relation to their catalytic activity for simultaneous hydrogen production under solar light. *Int. J. Hydrogen Energy* **2013**, *38*, 15992–16001. [CrossRef]
50. Gombac, V.; Sordelli, L.; Montini, T.; Delgado, J.J.; Adamski, A.; Adami, G.; Cargnello, M.; Bernal, S.; Fornasiero, P. CuO_x–TiO₂ Photocatalysts for H₂ Production from Ethanol and Glycerol Solutions. *J. Phys. Chem. A* **2010**, *114*, 3916–3925. [CrossRef]
51. Zhu, L.; Hong, M.; Ho, G.W. Fabrication of wheat grain textured TiO₂/CuO composite nanofibers for enhanced solar H₂ generation and degradation performance. *Nano Energy* **2015**, *11*, 28–37. [CrossRef]
52. Wang, Y.; Zhou, M.; He, Y.; Zhou, Z.; Sun, Z. In situ loading CuO quantum dots on TiO₂ nanosheets as cocatalyst for improved photocatalytic water splitting. *J. Alloys Compd.* **2020**, *813*, 152184. [CrossRef]
53. Zhuang, H.; Zhang, S.; Lin, M.; Lin, L.; Cai, Z.; Xu, W. Controlling interface properties for enhanced photocatalytic performance: A case-study of CuO/TiO₂ nanobelts. *Mater. Adv.* **2020**, *1*, 767–773. [CrossRef]